Technical Note: Noise models for virtual clinical trials of digital breast tomosynthesis

Lucas R. Borges[1,4,*], Bruno Barufaldi[2], Renato F. Caron[3], Predrag R. Bakic[2], Alessandro Foi[4], Andrew D. A. Maidment[2] and Marcelo A. C. Vieira[1]

[1]Department of Electrical and Computer Engineering, University of São Paulo, São Carlos, SP, 13566-590, Brazil

[2]Department of Radiology, University of Pennsylvania, PA, 19104, USA

[3]Barretos Cancer Hospital, Pio XII Foundation, Barretos, SP, 14784-400, Brazil

[4]Laboratory of Signal Processing, Tampere University, Tampere, 33720, Finland

[*] Corresponding author. E-mail: lucas.rodrigues.borges@usp.br

Address: 400 Av. Trabalhador São-Carlense, São Carlos, SP, 13566-590, Brazil

Abstract

Purpose: To investigate the use of an affine-variance noise model, with correlated quantum noise and spatially-dependent quantum gain, for the simulation of noise in virtual clinical trials (VCT) of digital breast tomosynthesis (DBT).

Methods: Two distinct technologies were considered: an amorphous-selenium (a-Se) detector with direct conversion, and a thallium doped cesium iodide (CsI(Tl)) detector with indirect conversion. A VCT framework was used to generate noise-free projections of a uniform 3D simulated phantom, whose geometry and absorption match those of a poly methyl methacrylate (PMMA) uniform physical phantom. The noise model was then used to generate noisy observations from the simulated noise-free data, while two clinically available DBT units were used to acquire projections of the PMMA physical phantom. Real and simulated projections were then compared using the signal-to-noise ratio (SNR) and normalized noise power spectrum (NNPS).

Results: Simulated images reported errors smaller than 4.4% and 7.0% in terms of SNR and NNPS, respectively. These errors are within the expected variation between two clinical units of the same model. The errors increase to 65.8% if uncorrelated models are adopted for the simulation of systems featuring indirect detection. The assumption of spatially-independent quantum gain generates errors of 11.2%.

Conclusions: The investigated noise model can be used to accurately reproduce the noise found in clinical digital breast tomosynthesis. The assumption of uncorrelated noise may be adopted if the system features a direct detector with minimal pixel crosstalk.

Keywords: noise simulation, quantum noise, electronic noise, virtual clinical trials, digital breast tomosynthesis

1   Introduction

The ultimate validation of medical devices is done through clinical trials. However, clinical trials require large financial investments for prototype design and patient recruiting. Furthermore, the duration of clinical trials is highly dependent on patient and physician availability. In this context, virtual clinical trials (VCTs) are becoming an attractive option as a pre-clinical validation [1–3].

In a VCT, the anatomical data, the imaging physics and human interpretation are simulated by computer algorithms.

To reproduce the image quality obtained in real-life systems accurately, it is vital to simulate the noise in VCTs accurately. For instance, noise can have higher impact on the detection of breast cancer than spatial resolution [4].

Here we investigate the validity of the noise models used to simulate digital breast tomosynthesis (DBT). We start by testing an affine-variance noise model with correlated quantum noise and spatially-varying quantum gain [5, 6], which we consider to be faithful to the detector physics. We then assess and compare the performance of simpler noise models.

2   Problem formulation

Our goal is to obtain approximations $\hat{z}(x)$ of observed DBT pixels $z(x)$, by adding noise to a simulated noise-free signal $y(x)$ generated by a VCT tool.

Let us consider $z(x)$ as an observed pixel of a raw DBT projection at spatial position $x \in \mathbb{Z}^2$. As in [5, 6], we model $z(x)$ as

$$z(x) \approx \hat{z}(x) = \lambda(x)\pi(x) + \tau + \omega_\mathrm{e}, \qquad \pi(x) \sim \mathcal{P}\{y(x)/\lambda(x)\}, \tag{1}$$

where $\mathcal{P}\{\xi\}$ is a Poisson distribution with average count ξ, describing the signal corrupted by heteroskedastic quantum noise; λ is the scaling of the Poisson noise, which is related to the quantum gain of the image formation and to the detector gain; y is the flat-fielded simulated underlying noise-free signal; τ is the pixel offset; and ω_e is the homoskedastic Gaussian noise, which represents the signal-independent noise sources, such as readout, amplification and thermal noise, here referred to as electronic noise. The coefficients λ vary with x, i.e. we account for the spatial dependency of the pixel gain, which results from the flat-fielding process that compensates non-uniformities such as described by the inverse square law and heel effect.

From (1), the expectation and variance of $z(x)$ depend on $y(x)$ and are

$$\mathrm{E}\{z(x)|y(x)\} = y(x) + \tau, \tag{2}$$
$$\mathrm{var}\{z(x)|y(x)\} = y(x)\lambda(x) + \sigma_\mathrm{e}^2. \tag{3}$$

In the model above, the variance is an affine function of $y(x)$, where $\lambda(x)$ is the slope and $\sigma_\mathrm{e}^2 = \mathrm{var}\{\omega_\mathrm{e}\}$ is the intercept. Hence, (2)-(3) is often referred to as a signal-dependent *affine-variance* noise model. Due to the counting range at which DBT systems operate ($y/\lambda \gg 10$), we assume that the quantum noise is approximately normally distributed [7].

Equation (1) may be described in the additive form

$$z(x) = y(x) + \tau + \omega_\mathrm{q} + \omega_\mathrm{e}, \tag{4}$$

where ω_q and ω_e are the signal-dependent and signal-independent noise components, respectively. Each noise component can be also represented as

$$\omega_\mathrm{q} = (\mathcal{K}_\mathrm{q} * \mathcal{N}\{0, 1\})\sqrt{\lambda y} \tag{5}$$
$$\omega_\mathrm{e} = (\mathcal{K}_\mathrm{e} * \mathcal{N}\{0, 1\})\sigma_\mathrm{e} \tag{6}$$

where $\mathcal{K}_q$ and $\mathcal{K}_e$ are convolution kernels that determine the spatial correlation of each noise component starting from the uncorrelated noise $\mathcal{N}\{\mu, \gamma\}$, normally distributed, with mean μ and variance γ. Both kernels must be normalized so that $||\mathcal{K}_q||_2 = ||\mathcal{K}_e||_2 = 1$, to conserve the variances of ω_q and ω_e.

Below we present two simplified noise models derived from the initial noise model described by (1)–(6).

- **Simplification 2.1:** The first simplification adopts a spatially-invariant λ, i.e. $\lambda(x) = \bar{\lambda}, \forall x$, where $\bar{\lambda}$ represents the average of λ over a region of interest (ROI). The average minimizes the quadratic discrepancies between $\bar{\lambda}$ and λ over the ROI. The common argument for this approximation is that often the breast only covers a small area of the detector where the variations of λ are smaller.

- **Simplification 2.2:** The second simplification assumes an affine-variance model with uncorrelated quantum noise, i.e. $\mathcal{K}_q = \delta(0)$. This assumption is commonly adopted for direct conversion detectors, due to the low pixel crosstalk reported by this technology.

3   Methods

Figure 1 illustrates the adopted validation strategy, with the noise simulation step described in detail. We started the validation by selecting appropriate poly methyl methacrylate (PMMA) uniform phantoms, commonly provided by the vendors for flat-fielding calibration. The PMMA phantom allows an easy estimation of the signal and noise properties due to the uniformity of the phantom. Digital 3D models of the physical phantoms were then generated with the first module of the VCT pipeline. The digital models were designed to reproduce the absorption and geometry of the PMMA physical phantoms.

Projections of the physical phantoms were acquired at a range of dose levels. Meanwhile, the VCT pipeline was used to generate simulated noise-free DBT projections, considering the same acquisition geometry and selected radiographic factors from the clinical units. The presented noise models were then used to generate noisy projections, which were compared to the projections obtained from the clinical units.

4   Materials

Clinical images were acquired using DBT systems from two vendors. Table 1 presents the properties of both systems.

Two PMMA physical phantoms were used during the experiments. One of them, with 4 cm thickness, was provided by the manufacturer of the Selenia Dimensions system. The second phantom, with 3 cm thickness, was provided by the manufacturer of the Senographe Essential system. The uniform phantoms are commonly used for the flat-fielding correction and they simplify the estimation of signal and noise properties at each spatial position.

Simulations were performed using the virtual clinical trial framework developed at the University of Pennsylvania [8,9], and available for download [10]. This VCT tool is dedicated to the optimization and validation of breast imaging modalities and is capable of simulating the anatomy of the human breast tissue, the physics of the x-rays generation, transmission and detection, and the psychophysics behind image interpretation.

The simulation assumed perfectly flat-fielded projections. The *Siddon* 3D algorithm [11] was adopted as the x-ray tracing algorithm. The effects of lag/ghosting and scatter were not considered in the ray-tracing. Lag/ghosting and scatter respectively affect the average pixel value reported at different angles and the noise power spectrum. Thus there might be minor

intensity differences between the real and simulated phantom projections, which were partly compensated by the affine mapping of intensities as done in [12, 13]. The noise power spectral density (PSD) is estimated from real data and thus naturally includes scattering effects.

Two digital phantoms were generated, both designed to mimic the absorption and geometry of the two uniform PMMA physical phantoms.

4.1   Image Acquisition

Two image sets were required from each of the two system models: one calibration set and one validation set. The calibration set was used to estimate noise parameters of the DBT systems, such as τ, λ, σ_{e}, $\mathcal{K}_{\mathrm{q}}$ and $\mathcal{K}_{\mathrm{e}}$; while the validation set was used to estimate the fidelity between real and simulated noise considering a range of radiation doses. To avoid circular proofing, calibration and validation sets were acquired from two different units of the same model. Thus, a total of four clinical units were used for the image acquisition process. Table 2 presents the radiographic factors used during the acquisition process. Ten realizations were acquired at each combination of radiographic factors in the validation sets to allow better noise estimation.

As we adopted distinct units for calibration and validation, it is important to investigate the SNR and NNPS variability between systems of the same model. For this purpose, we acquired ten extra sets of projections using the calibration systems at 30 and 63 mAs on the a-Se and CsI(Tl) systems, respectively. The extra sets were used to estimate the variability in SNR and NNPS between the calibration and validation systems.

Conventional DBT images were acquired on both systems. The PMMA phantoms were positioned on the breast support. Projections from Selenia Dimensions and Senographe Essential were acquired without and with an anti-scatter grid, respectively, as per the systems' default. Only raw (DICOM tag "for processing") projections were used in this study.

4.2   Paramenter Estimation

Below we specify the methods adopted to estimate the noise parameters. It is important to emphasize that the estimation methods were used as tools, and thus we refer the readers to the cited works to find detailed descriptions about the estimation process.

- **Pixel Offset** τ: estimated using the mean pixel value (MPV) $\times$ incident air kerma (IAK) plot as described by the EUREF [14]. A 10 mm $\times$ 10 mm square ROI used for the estimation was taken from each raw projection, at the midline, 60 mm from the chest wall edge. A single τ was estimated for each system model. The estimated offset values are close to the reported by other works [15, 16].

- **Standard Deviation of the Electronic Noise** σ_{e}: estimated using the noise variance $\times$ linearized MPV plot. The linearized MPV was calculated by subtracting the offset τ from the raw pixel values, and σ_{e} was estimated as the square root of the intercept of the affine function fitted to the noise variance $\times$ linearized MPV plot. The ROIs were chosen as described previously. A single σ_{e} was estimated for each system model.

- **Correlation Kernel of the Electronic noise** $\mathcal{K}_{\mathrm{e}}$: throughout this paper we assume that the electronic noise is not correlated, i.e. $\mathcal{K}_{\mathrm{e}} = \delta(0)$. This assumption is based on measurements performed by other authors on both a-Se [17] and CsI(Tl) [15] detectors.

- **Gain Map of the Quantum Noise** λ: estimated using the ratio between the variance of the quantum noise and the linearized MPV, as described in [6, 12]. The estimated map was detrended using a second order polynomial surface. The estimation was performed

in each projection and each combination of radiographic factors from the calibration sets. The estimates were then averaged among radiographic factors. Thus, a single λ map was estimated for each projection angle of each system.

- **Correlation Kernel of the Quantum Noise** $\mathcal{K}_q$: estimated through the power spectral density as in [6,12] over the calibration image with the highest dose, so that the quantum noise dominates over the electronic one. 200 rows and columns of pixels were excluded from each border to avoid saturated pixels.

Table 3 shows the estimated pixel offset and standard deviation (std) of the electronic noise. Figure 2 shows examples of estimated λ maps and blurring kernels $\mathcal{K}_q$, taken from the central projection. The two λ maps shown in Figure 2 make evident the impact of the non-uniformity correction on the gain of the quantum fraction of the noise. The shape of the maps resemble the shape seen in the non-uniformities described by the inverse square law and heel effect.

The analysis of the cross-section taken from the 2D kernel shows that the a-Se detector has 99.8% of its energy concentrated at the central pixel, and 0.2% of its energy spreading to the neighboring pixels. Meanwhile, the CsI(Tl) detector has 83.9% of its energy concentrated at the central pixel, with 16.1% of energy spreading to the neighboring pixels.

4.3 Metrics

Several works have studied noise in breast imaging [4,5,18–22]. Noise is usually evaluated by the signal-to-noise ratio (SNR), the signal difference-to-noise ratio (SDNR), or the normalized noise power spectrum (NNPS). Here we adopt the local SNR and NNPS as reasonable descriptors of the noise statistics in DBT systems. The local SNR is the pointwise ratio between the local signal mean and the local noise standard deviation, estimated over ten realizations

$$SNR(x) = \frac{\mu(x)}{\sqrt{\sigma(x)^2}}, \qquad \mu(x) = \frac{1}{R}\sum_{r=1}^{R} z_r(x), \qquad \sigma^2(x) = \frac{1}{R-1}\sum_{r=1}^{R}(z_r(x) - \mu(x))^2, \quad (7)$$

where $r = 1, 2, \ldots, R$ are realizations of the image ($R = 10$). For each pair of real and simulated data, the overall average SNR was plotted as a function of projection angle. SNR profiles were also plotted by averaging the SNR map in the chest-wall-to-nipple (posterior-anterior, PA) and lateral directions.

The spectral properties of the simulated and real noise were compared in terms of normalized noise power spectrum (NNPS) [23, 24], which is defined as

$$NPS = \frac{Ns^2}{M}\sum_{m=1}^{M}|\mathcal{F}\{I_m - S_m\}|^2, \qquad NNPS = \frac{NPS}{L^2}, \quad (8)$$

where N is the number of pixels in a patch, s is the pixel size, $m = 1, \ldots, M$ indicates the patch taken from the uniform image I, $\mathcal{F}$ indicates the Fourier transform, I_m and S_m are the signal and detrending surface of the patch m, respectively, and L is the average value of I. We adopted the mean value of the patch m as the detrending S_m. Because of the detrending using smooth trend, low frequencies of the power spectrum cannot be estimated. Thus, frequencies below 0.5 mm^{-1} were omitted from the graphs.

The overall quality of the noise simulation was computed as the pointwise relative absolute error between simulated and real SNR maps. Second-order polynomial surfaces were fitted to each SNR map to minimize noise from the estimations due to the few realizations. We opted to calculate the errors over the entire detector field, as in clinical practice there are many breasts that are larger than the detector, sometimes even requiring tiling of the breast.

5 Results

Figure 3 shows examples of simulated and real noise maps, with a magnified portion for better visual assessment. The SNR and NNPS obtained for both systems at a range of dose levels are shown in Figure 4. The PA and lateral SNR profiles make evident the exponential and quadratic behavior of the SNR in each of the two directions, respectively. Furthermore, the NNPS shows that the noise from the a-Se detector has an approximately flat spectrum, when compared to the CsI(Tl) detector.

Table 4 summarizes the relative SNR and NNPS results obtained with the initial noise model (1)–(6) and the Simplifications 2.1 and 2.2, along with the respective 95% confidence intervals as the values in parentheses. Assuming uncorrelated noise impacted mostly the NNPS of the CsI(Tl) detector but did not affect any of the SNR values.

The system variability study showed that the a-Se detector at 30 mAs yielded an average discrepancy of 3.2% (2.0% 4.4%) in terms of SNR, and 3.8% (2.5% 5.2%) in terms of NNPS. Considering the CsI(Tl) detector at 63 mAs, the estimated variability was 3.5% (3.0% 4.0%) in terms of SNR, and 7.6% (5.3% 9.9%) in terms of NNPS. Thus, the errors achieved by our simulations are comparable to the system variability.

6 Discussions and Conclusions

We evaluated the similarity between real and simulated noise in DBT projections generated by a virtual clinical trials framework. The initial noise model accounts for the correlation of the quantum noise and the spatial dependency of the quantum gain λ. Two simplified versions of the initial noise model were also investigated. Structural noise was considered negligible at the the counting ranges at which DBT operates, and thus it was not considered here.

Noise maps are illustrated in Figure 3, where we can appreciate the noise correlation of the CsI(Tl) detector. This correlation results from the indirect energy conversion to visible light adopted by this technology.

In Figure 4, noise measurements from the central projection are plotted as an example. The PA plot of the SNR illustrates how this measurement changes significantly as the distance to the chest wall increases. This is a result of the calibration process (flat-fielding), which compensates non-uniformities described by the inverse square law and the heel effect. The NNPS shows that the CsI(Tl) detector indeed yield much stronger noise correlation, compared to the a-Se detector.

The results of this study are summarized in Table 4. The errors in the simulation are comparable to the discrepancy between systems of the same model.

The assumption of spatially-independent quantum gain λ resulted in minor differences in the NNPS measurements, since this quantity does not carry spatial information. However, the average error was significantly increased in terms of SNR, reaching up to 11.2%.

Lastly, the assumption of uncorrelated quantum noise had virtually no impact in the simulated noise of the a-Se detector. However, significant errors (up to 65.8%) arise when this model is adopted for the CsI(Tl) detector.

Monte Carlo (MC) methods provide a gold-standard approach to simulating noisy x-ray projections. Recent works [25, 26] showed that a MC-based method, as well as the single iteration x-ray tracing used here, are capable of reproducing the outcome of real-life DBT clinical trials using exclusively artificial data. However, even though both methods perform with an acceptable degree of realism, the computational time required by MC-based methods [25] is up to 65 times higher than required by the algorithm adopted here [27]. As virtual clinical trials may involve large numbers of simulations (potentially $10^4 - 10^5$ simulated images), our goal is to develop a rapid alternative with sufficient realism to obtain accurate results.

The SNR and NNPS ranges of the two detectors are considerably different, as the Senographe Essential unit could not be set to current-time products lower than 36 mAs. Thus, SNR and NNPS should not be used for a direct comparison of the systems' performance.

Our analysis can be extended to other imaging modalities that share a similar noise model with DBT.

In conclusion, we have investigated the fidelity between simulated and real noise measurements from two DBT systems. An affine-variance noise model, which considers the correlation of the quantum noise and the spatial dependency of the quantum gain was able to achieve errors as small as the variability found between systems of the same model. The correlation of the quantum noise may be disregarded if simulating the noise from a direct detector with minimal pixel crosstalk.

Acknowledgements

References

[1] B. Zhao, J. Zhou, Y.-H. Hu, T. Mertelmeier, J. Ludwig, and W. Zhao, "Experimental validation of a three-dimensional linear system model for breast tomosynthesis," *Medical physics*, vol. 36, no. 1, pp. 240–251, 2009.

[2] I. Sechopoulos and C. Ghetti, "Optimization of the acquisition geometry in digital tomosynthesis of the breast," *Medical physics*, vol. 36, no. 4, pp. 1199–1207, 2009.

[3] S. Young, P. R. Bakic, K. J. Myers, R. J. Jennings, and S. Park, "A virtual trial framework for quantifying the detectability of masses in breast tomosynthesis projection data," *Medical physics*, vol. 40, no. 5, 2013.

[4] R. S. Saunders, J. A. Baker, D. M. Delong, J. P. Johnson, and E. Samei, "Does image quality matter? Impact of resolution and noise on mammographic task performance," *Medical Physics*, vol. 34, no. 10, pp. 3971–3981, 2007.

[5] A. Burgess, "On the noise variance of a digital mammography system," *Medical physics*, vol. 31, no. 7, pp. 1987–1995, 2004.

[6] L. R. Borges, I. Guerrero, P. R. Bakic, A. Foi, A. D. Maidment, and M. A. C. Vieira, "Method for simulating dose reduction in digital breast tomosynthesis," *IEEE Transactions on Medical Imaging*, vol. 36, no. 11, pp. 2331–2342, 2017.

[7] F. A. Haight, *Handbook of the Poisson distribution.* Wiley, 1967.

[8] A.-K. Carton, P. R. Bakic, C. Ullberg, H. Derand, and A. D. Maidment, "Development of a physical 3D anthropomorphic breast phantom," *Medical physics*, vol. 38, no. 2, pp. 891–896, 2011.

[9] D. D. Pokrajac, A. D. Maidment, and P. R. Bakic, "Optimized generation of high resolution breast anthropomorphic software phantoms," *Medical physics*, vol. 39, no. 4, pp. 2290–2302, 2012.

[10] P. R. Bakic, D. Higginbotham, B. Barufaldi, and A. D. A. Maidment. Openvct: The open-source virtual clinical trial project. [Online]. Available: https://sourceforge.net/projects/openvct/

[11] R. L. Siddon, "Prism representation: a 3d ray-tracing algorithm for radiotherapy applications," *Physics in Medicine & Biology*, vol. 30, no. 8, p. 817, 1985.

[12] L. R. Borges, L. Azzari, P. R. Bakic, A. D. Maidment, M. A. C. Vieira, and A. Foi, "Restoration of low-dose digital breast tomosynthesis," *Measurement Science and Technology*, vol. 29, no. 6, 2018.

[13] G. Boracchi and A. Foi, "Uniform motion blur in poissonian noise: Blur/noise tradeoff," *IEEE Transactions on Image Processing*, vol. 20, no. 2, pp. 592–598, 2011.

[14] R. van Engen, R. Bouwman, D. Dance, P. Heid, B. Lazzari, N. Marshall, S. Schopphoven, C. Strudley, M. Thjissen, and K. Young, "Protocol for the quality control of the physical and technical aspects of digital breast tomosynthesis system," *EUREF, European Guidelines for Quality Assurance in Breast Cancer Screening and Diagnosis*, 2013.

[15] C. Ghetti, A. Borrini, O. Ortenzia, R. Rossi, and P. L. Ordóñez, "Physical characteristics of GE Senographe Essential and DS digital mammography detectors," *Medical physics*, vol. 35, no. 2, pp. 456–463, 2008.

[16] C. Strudley, P. Looney, and K. Young, "Technical evaluation of Hologic Selenia Dimensions digital breast tomosynthesis system (NHSBSP equipment report 1307 version 2)," *Sheffield: NHS Cancer Screening Programmes*, 2014.

[17] A. Mackenzie, N. W. Marshall, A. Hadjipanteli, D. R. Dance, H. Bosmans, and K. C. Young, "Characterisation of noise and sharpness of images from four digital breast tomosynthesis systems for simulation of images for virtual clinical trials," *Physics in Medicine & Biology*, vol. 62, no. 6, p. 2376, 2017.

[18] X. Gong, S. J. Glick, B. Liu, A. A. Vedula, and S. Thacker, "A computer simulation study comparing lesion detection accuracy with digital mammography, breast tomosynthesis, and cone-beam CT breast imaging," *Medical physics*, vol. 33, no. 4, pp. 1041–1052, 2006.

[19] W. Huda, A. M. Sajewicz, K. M. Ogden, and D. R. Dance, "Experimental investigation of the dose and image quality characteristics of a digital mammography imaging system," *Medical Physics*, vol. 30, no. 3, p. 442, 2003.

[20] W. Zhao, W. Ji, A. Debrie, and J. Rowlands, "Imaging performance of amorphous selenium based flat-panel detectors for digital mammography: Characterization of a small area prototype detector," *Medical physics*, vol. 30, no. 2, pp. 254–263, 2003.

[21] T. Wu, R. H. Moore, E. A. Rafferty, and D. B. Kopans, "A comparison of reconstruction algorithms for breast tomosynthesis," *Medical physics*, vol. 31, no. 9, pp. 2636–2647, 2004.

[22] A. Haus and M. Yaffe, "Screen-film and digital mammography. Image quality and radiation dose considerations," *Radiologic Clinics of North America*, vol. 38, no. 4, pp. 871–898, July 2000.

[23] I. Cunningham, "Applied linear-system theory," in *Handbook of Medical Imaging: Physics and Psychophysics*, R. van Metter, J. Beutel, and H. Kundel, Eds. SPIE, 2000, pp. 79–155.

[24] J. T. Dobbins III, "Image quality metrics for digital systems," in *Handbook of Medical Imaging: Physics and Psychophysics*, R. van Metter, J. Beutel, and H. Kundel, Eds. SPIE, 2000, pp. 79–155.

[25] A. Badano, C. G. Graff, A. Badal, D. Sharma, R. Zeng, F. W. Samuelson, S. J. Glick, and K. J. Myers, "Evaluation of digital breast tomosynthesis as replacement of full-field digital mammography using an in silico imaging trial," *JAMA Network Open*, vol. 1, no. 7, pp. e185 474–e185 474, 2018.

[26] P. R. Bakic, B. Barufaldi, D. Higginbotham, S. P. Weinstein, A. N. Avanaki, K. S. Espig, A. Xthona, T. R. Kimpe, and A. D. Maidment, "Virtual clinical trial of lesion detection in digital mammography and digital breast tomosynthesis," in *Medical Imaging 2018: Physics of Medical Imaging*, vol. 10573. International Society for Optics and Photonics, 2018, p. 1057306.

[27] B. Barufaldi, D. Higginbotham, P. R. Bakic, and A. D. Maidment, "Openvct: a gpu-accelerated virtual clinical trial pipeline for mammography and digital breast tomosynthesis," in *Medical Imaging 2018: Physics of Medical Imaging*, vol. 10573. International Society for Optics and Photonics, 2018, p. 1057358.

Figures and Tables

Table 1: Properties of the two simulated system models.

Model	Detector	Pixel Size	# of Projections	Angular Range
Selenia Dimensions	a-Se	140μm	15	15°
Senographe Essential	CsI(Tl)	100μm	9	25°

Table 2: Radiographic factors used during the image acquisition process.

Detector	Target/Filter	kVp	PMMA	Total mAs	Application
a-Se	W/Al	31	4 cm	69, 63, 54, 48, 45	Calibration
				60, 30, 15, 9	Validation
CsI(Tl)	Rh/Rh	29	3 cm	120, 90, 72, 54, 45, 36	Calibration
				99, 81, 63, 54, 36	Validation

Table 3: Estimated pixel offset and standard deviation (std) of the electronic noise.

Detector	Pixel Offset (τ)	Electronic Noise Std (σ_{e})
a-Se	47	1.37
CsI(Tl)	-17	7.03

Table 4: Relative error between simulated and real noise measurements. The values in parenthesis represent the 95% confidence interval of the measurements.

| Detector	mAs	Initial Model (Sec. 2) SNR (%)	NNPS (%)	$\lambda(x) = \bar{\lambda}, \forall x$ SNR (%)	NNPS (%)	$\mathcal{K}_{\mathrm{q}} = \delta(0)$ SNR (%)	NNPS (%)
a-Se	60	4.4 (4.0 4.9)	6.1 (5.5 6.1)	11.1 (10.8 11.3)	9.8 (8.8 10.8)	4.4 (4.0 4.9)	5.4 (4.0 6.8)
	30	2.2 (1.7 2.7)	3.4 (2.6 4.2)	11.2 (9.7 11.7)	9.8 (8.7 10.9)	2.2 (1.7 2.7)	5.7 (4.2 7.1)
	15	1.4 (1.2 1.6)	1.8 (1.1 2.6)	11.0 (10.8 11.1)	4.9 (4.4 5.5)	1.4 (1.2 1.6)	5.0 (3.5 6.5)
	9	2.9 (2.7 3.1)	5.8 (5.0 6.6)	11.1 (11.0 11.2)	2.7 (1.8 3.6)	2.9 (2.7 3.1)	8.9 (6.8 11.1)
CsI(Tl)	99	3.9 (3.7 4.2)	7.0 (4.9 9.1)	6.9 (6.5 7.3)	7.2 (4.9 9.4)	3.9 (3.7 4.2)	65.8 (50.0 81.6)
	81	3.6 (3.4 3.9)	6.3 (4.2 8.4)	6.8 (6.4 7.2)	6.3 (4.2 8.4)	3.6 (3.4 3.9)	65.1 (49.7 80.6)
	63	3.0 (2.7 3.4)	6.0 (3.4 8.6)	6.8 (6.3 7.1)	5.8 (3.3 8.3)	3.0 (2.7 3.4)	63.9 (48.8 79.0)
	54	2.8 (2.3 3.4)	5.4 (2.8 8.0)	6.3 (5.6 7.0)	5.5 (3.0 8.0)	2.8 (2.3 3.4)	62.3 (47.9 76.8)
	36	3.7 (3.4 3.9)	5.2 (1.9 8.5)	4.5 (4.2 4.8)	5.0 (2.1 7.9)	3.7 (3.4 3.9)	61.0 (46.9 75.0)
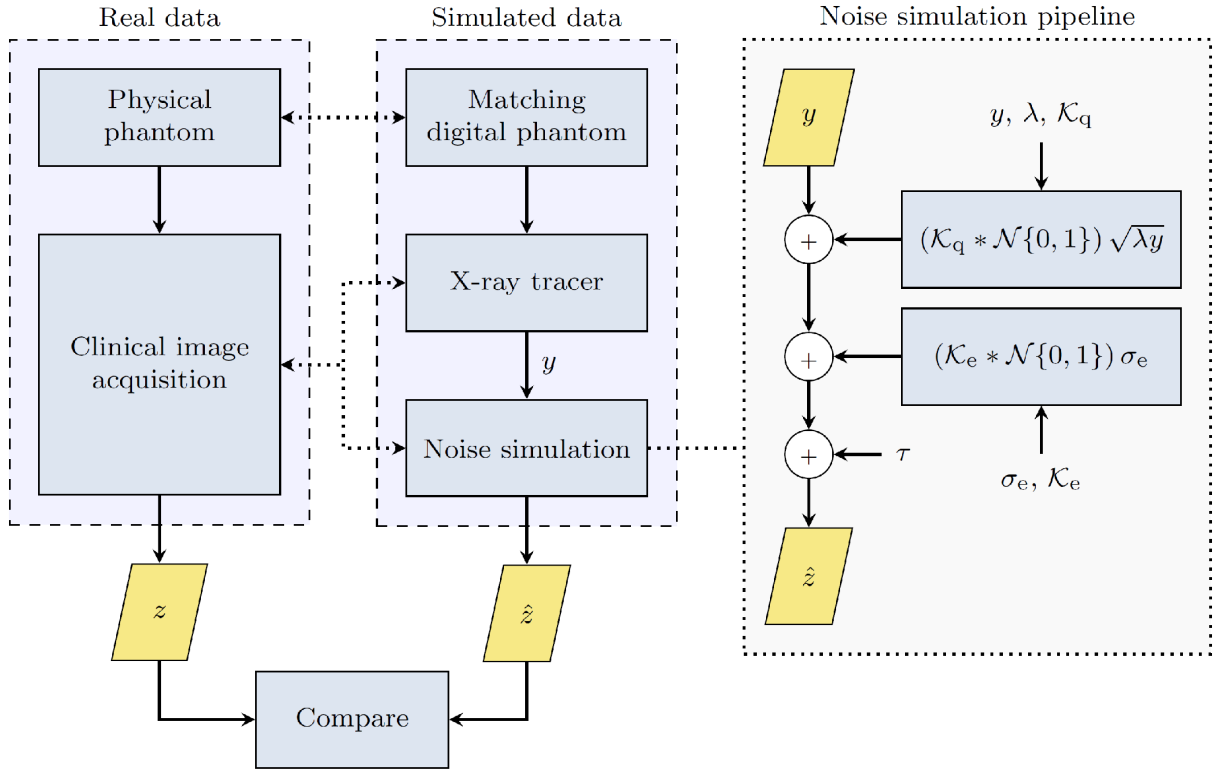
Figure 1: Overview of the adopted validation process. The variable y represents the flat-fielded noise-free simulated projection generated by a VCT framework. The rightmost flowchart illustrates the noise simulation pipeline. The methods adopted to estimate τ, λ, σ_{e}, $\mathcal{K}_{\mathrm{q}}$ and $\mathcal{K}_{\mathrm{e}}$ are referenced in Section 4.2.
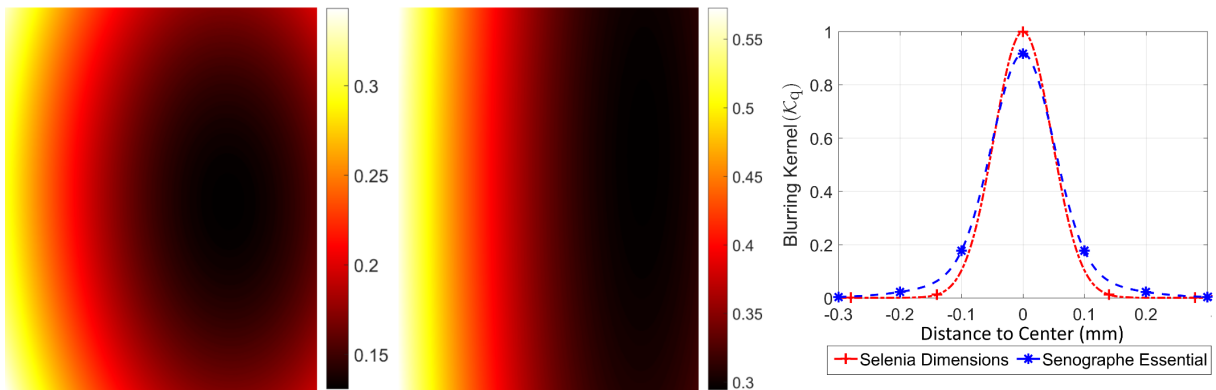
Figure 2: From left to right: estimated λ at the central projection from a-Se and CsI(Tl) detectors, respectively, and the cross-section of the 2D kernel $\mathcal{K}_{\mathrm{q}}$ from both detectors. Markers represent the experimental data, while the lines represent a Gaussian fit of the data.
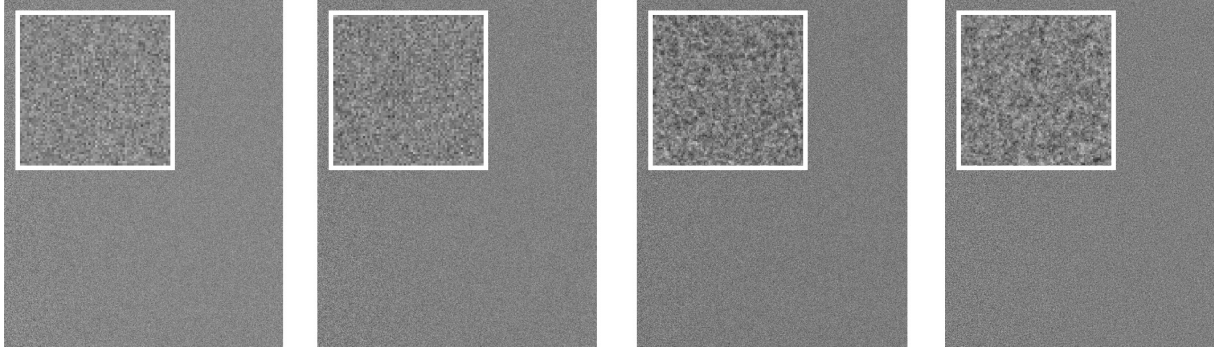
Figure 3: Noise maps taken from the central projection. From left to right: real (a-Se, 60 mAs), simulated (a-Se, 60 mAs), real (CsI(Tl), 63 mAs) and simulated (CsI(Tl), 63 mAs). The noise maps were estimated as the difference between two realizations of the image acquisition, divided by the square root of two, to correct the standard deviation.
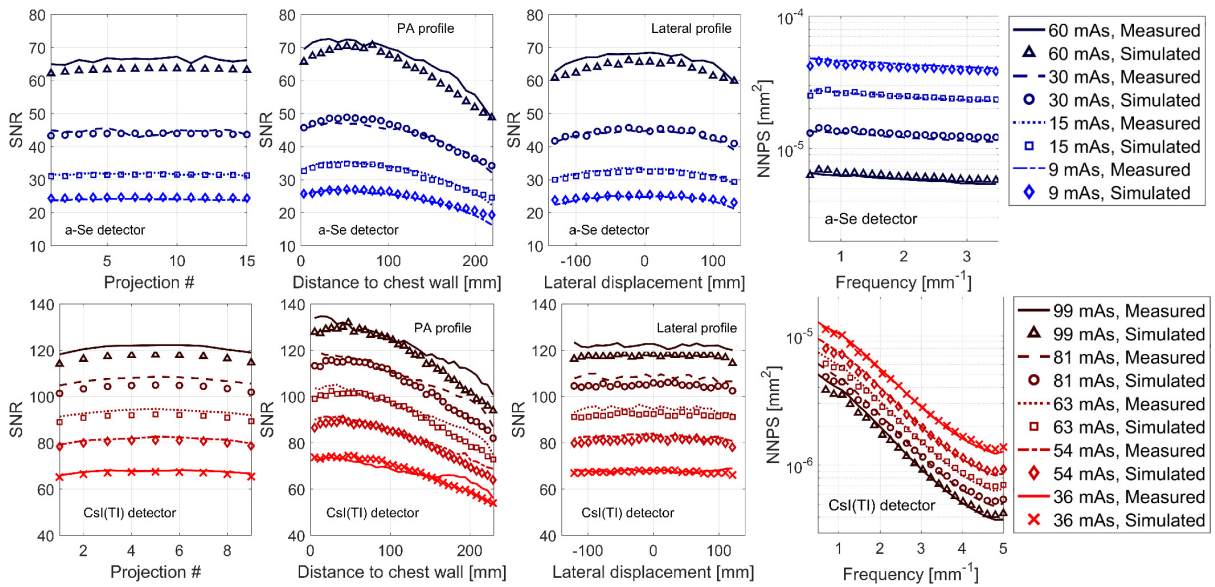

Figure 4: Examples of noise measurements from both detectors, simulated using the initial model described in Section 2 (top row: a-Se detector; bottom row: CsI(Tl) detector). The posterior-anterior (PA) SNR profiles, lateral SNR profiles, and the NNPS correspond to the central projection.